Controlling the Orientation of Semicrystalline Polymers by Crystallization in Magnetic Fields

Florian Ebert and Thomas Thurn-Albrecht*

Physikalisches Institut, Albert-Ludwigs-Universität Freiburg, Hermann-Herder-Strasse 3, 79104 Freiburg, Germany

Received June 5, 2003; Revised Manuscript Received August 15, 2003

ABSTRACT: Using X-ray scattering complemented by microscopic methods, we studied the alignment of a semicrystalline polymer—isotactic polystyrene—by crystallization in a high magnetic field (7 and 11 T). As reported previously, strong orientation of crystalline chain segments perpendicular to the magnetic field can be achieved. We present a method to determine the degree of orientation from the wide-angle X-ray scattering pattern in a quantitative way. The degree of orientation strongly depends on the crystallization temperature, allowing for nearly perfect orientation only at low supercooling. Furthermore, it is strongly influenced by the number of nuclei initiating spherulitic crystalline growth. Only for high nucleation density, such as that achieved by self-seeding, is strong macroscopic orientation obtained. Microscopic inspection of samples with a low number of nuclei shows that the magnetic field orients only the central part of large spherulites and the orientation is lost in the outer part of the spherulites; alignment takes place only in the initial stage of growth of a spherulite. The strong effect of the temperature of crystallization indicates a competition between orientation and growth.

Introduction

The possibility to control orientation in soft materials on a molecular scale by external fields is a very attractive feature, which in the case of liquid crystals has led to important technological applications. It has also been demonstrated recently that the ability to control small-scale structure in polymers by electric fields is potentially interesting for creating artificial nanostructures.[1−3] Generally, the orienting effect of the external fields, whether magnetic or electric, on an individual molecule is weak, and even for strongly anisotropic molecules the corresponding energies are usually small compared to the thermal energy. The strong effects observed in some cases, such as in the nematic liquid crystals mentioned above, rely on an effective amplification of the molecular anisotropy by preexisting ordered domains whose molecular mobility in the ordered state is high enough to enable a fast response to the external field. Although polymer crystals certainly exhibit an anisotropic diamagnetic susceptibility, their ability to rearrange internally is thought to be negligible compared to that of a liquid-crystalline material. The observation that semicrystalline polymers orient if they are crystallized in the presence of a strong magnetic field is therefore somewhat surprising.[4,5] This observation has now been confirmed for a number of different semicrystalline polymers.[6−10] In all cases, the alignment took place during the induction period (i.e., in the initial phase of crystallization during which a macroscopic crystallinity cannot yet be detected). It was suggested that the magnetic field acts on locally ordered structures in the melt, which are left over after melting.[8−10] This idea suggests that magnetic field-induced orientation might be related to the well-known process of self-seeding (i.e., the fact that for many semicrystalline polymers there exists a temperature range above the apparent melting temperature, such as that observed in a calorimetric experiment, in which small crystal fragments survive and then act as nucleation centers in a subsequent crystallization).[11]

Here we present a detailed study of the crystallization of isotactic polystyrene (iPS) in magnetic fields relating the orientation phenomena to characteristic features of crystal growth in polymer melts. We studied the influence of a broad set of parameters on the resulting degree of orientation and investigated the resulting structure on a variety of length scales using optical microscopy as well as X-ray scattering and electron microscopy. We show that the magnetic field has an appreciable influence only during the initial phase of growth of a spherulite. The branching processes leading to the formation of spherulites are not altered by the presence of the field. As a consequence, high nucleation density achieved by self-seeding is critical to achieve macroscopic orientation. Concerning the mechanism of orientation, most observations can be explained by the alignment of the hedritic cores of the spherulites during growth. No fully satisfactory explanation is currently available for the surprisingly short time within which alignment takes place. This discrepancy and possible consequences concerning the nature of the crystallization process are discussed in detail.

Theory

Field Effects. The magnetic contribution to the free energy of an object of volume V with a diamagnetic susceptibility tensor $\tilde{\chi}$ in a magnetic field $\vec{H}$ can be expressed as

$$G_{\mathrm{mag}} = \frac{-\mu_0 V \vec{H} \tilde{\chi} \vec{H}}{2} \tag{1}$$

where μ_0 is the vacuum permeability. For crystalline iPS[12,13] with its hexagonal unit cell, one principal axis of $\tilde{\chi}$ is parallel $\vec{c}$, which also corresponds to the direction of the chain axis (eigenvalue $\chi_{\parallel}$). The other two axes can be chosen in any direction orthogonal to $\vec{c}$ (common

* To whom correspondence should be addressed. Present address: Martin-Luther-Universität Halle-Wittenberg, Fachbereich Physik, 06099 Halle, Germany. E-mail: thurn-albrecht@physik.uni-halle.de.

10.1021/ma034760g CCC: $25.00
Published on Web 10/17/2003

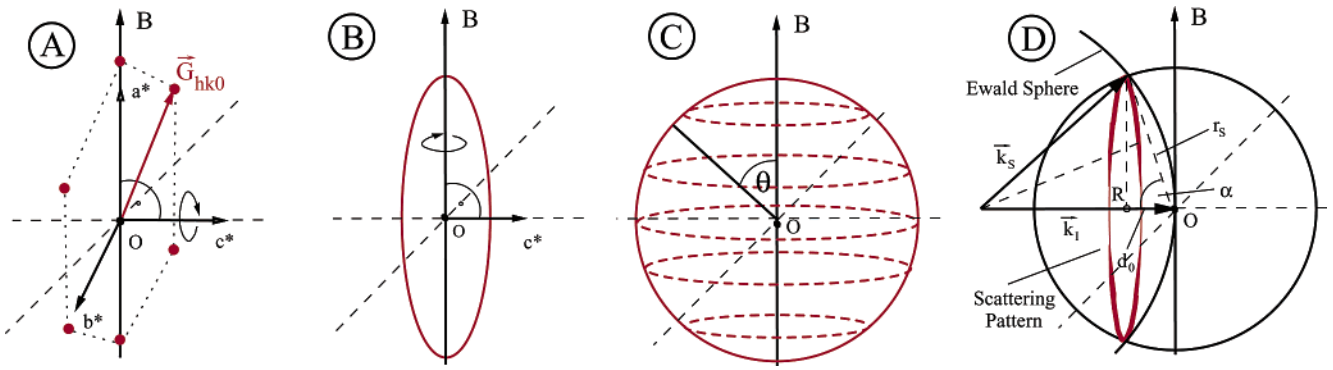

Figure 1. Reciprocal space construction of the scattering pattern caused by an (*hk*0) reflection as it is observed in a WAXS measurement of a uniaxially oriented sample with perfect orientation $\vec{c} \perp \vec{B}$ and no preferred orientation of axes $\vec{a}$ and $\vec{b}$ within the plane normal to $\vec{c}$. A hexagonal unit cell is assumed.

Table 1. Low-Order Bragg Reflections of Isotactic Polystyrene[a]

Bragg reflection (*hkl*)	Bragg angle 2θ (deg)
(110)	8.20
(300)	14.24
(220)	16.56
(211)	18.14
(410)/(311)	21.27/21.44

[a] Reflections (410)/(311) could not be separated in our measurements because of limited resolution.

eigenvalues $\chi_a = \chi_b = \chi_\perp$). In this case, eq 1 can be written as

$$G_{mag}(\theta) = \frac{-VB^2\Delta\chi \cos^2\theta}{2\mu_0} \qquad (2)$$

with $\Delta\chi = \chi_{||} - \chi_\perp$. θ denotes the angle between the magnetic field and the *c* axis. For iPS, $\Delta\chi$ is negative, resulting in a state of lowest free energy for $\theta = \pi/2$ (i.e., at equilibrium, the chain axis is oriented perpendicular to the direction of $\vec{B}$). A simple estimate shows that for typical parameters in our experiment ($B = 7$ T, $T = 210$ °C), $\Delta G = |G(0) - G(\pi/2)| = VB^2|\Delta\chi|/2\mu_0$ becomes comparable to thermal energy kT only for a volume as large as $V \approx (70\ \text{nm})^3$. Here we used $\Delta\chi \approx -8.15 \times 10^{-7}$, an estimate based on the assumption that the diamagnetic susceptibility is dominated by the contribution of the phenyl rings.[32] Obviously, the magnetic field can exert an appreciable effect only on relatively large anisotropic aggregate structures.

Scattering from Magnetically Aligned Isotactic Polystyrene. Isotactic polystyrene forms a crystal with a hexagonal unit cell (lattice parameters: $a = b = 22.08$ Å, $c = 6.63$ Å). Observable low-order Bragg reflections are given in Table 1.

The wide-angle X-ray scattering pattern of a semicrystalline polymer with uniaxial symmetry, for which the orientation is determined by the condition that one crystal axis (here the *c* axis) aligns perpendicular to a given direction (here defined by the magnetic field $\vec{B}$), is more complex than a usual fiber pattern. We briefly describe the typical patterns encountered. The construction of the pattern caused by an (*hk*0) Bragg reflection can be broken down into steps that are illustrated in Figure 1. For a hexagonal lattice as in the case of iPS, the reciprocal lattice is also hexagonal, with $\vec{c}^*$ being parallel to $\vec{c}$ and $\vec{a}^*$ and $\vec{b}^*$ lying in the same plane as $\vec{a}$ and $\vec{b}$. In Figure 1A, the location of the 6-fold G_{hk0} reflection is shown for a given orientation of $\vec{c}^*$ perpendicular to $\vec{B}$. Because there is no preferred orientation of $\vec{a}$ and $\vec{b}$ and no preferred direction perpendicular to $\vec{B}$, two averages have to be performed. The first corresponds to a rotation around $\vec{c}^*$, and the second consists of a rotation of the resulting pattern around the direction of $\vec{B}$. The result of this procedure is illustrated in Figure 1B and C, leading to a nonhomogeneous distribution of the intensity on a sphere. Specifically, the intensity distribution $i(\theta)$ in reciprocal space is indirectly proportional to the circumference of the circles indicated by the broken lines in Figure 1C (i.e., $i(\theta) \propto 1/\sin\theta$). The scattering pattern observed in an experiment consists of the intersection of the intensity distribution in reciprocal space with the Ewald sphere, defined by the wave vectors $\vec{k}_I$ and $\vec{k}_S$ of the incident and the scattered beam, respectively, as illustrated in Figure 1D. This intersection consists of a ring with an inhomogeneous intensity distribution proportional to $i(\theta)$. An azimuthal scan over the ring corresponding to a given (*hk*0) reflection shows two peaks along the direction of the magnetic field (azimuthal angle $\phi = 0$ and $\phi = \pi$) with a finite width and a finite offset, even for perfect orientation. The pattern corresponding to an (*hkl*) reflection can be understood analogously and is illustrated in Figure 2. Here, the rotation around $\vec{c}^*$ (Figure 2A and B) first distributes the intensity on two circles a distance $l \cdot |\vec{c}^*|$ from the origin of reciprocal space. Rotation around $\vec{B}$ (Figure 2C) distributes the intensity on a belt around the equator of the sphere corresponding to the reflection. Again, the intensity $i(\theta)$ depends on θ and is higher on the edges of the belt than on the equator. The intersection with the Ewald sphere leads to an azimuthal intensity distribution as shown schematically in Figure 2D. The pattern that would be observed for a (00*l*) reflection is obtained as a special case. The two circles shown in Figure 2B are reduced to two points on the $\vec{c}^*$ axis, and the belt of Figure 2C becomes a circle on the equator. In the experiment, two equatorial spots would be observed. A quantitative description of the pattern caused by an (*hk*0) reflection is given in the Appendix.

Experimental Section

Sample. High molecular weight isotactic polystyrene (iPS) was purchased from Aldrich Chemical Co. The semicrystalline sample shows a glass transition around $T_g \approx 100$ °C and a broad melting range (~170−215 °C). The equilibrium melting point of iPS is $T_m^\infty = 289$ °C.[15] All samples used in this study were melt pressed at 250 °C and then cooled to $T_c = 170$ °C, at which temperature they were kept for 2 h, sufficiently long to achieve full crystallization. The samples for scattering experiments had a thickness of 0.5 mm; for optical microscopy, samples with a thickness of 25 μm were used.

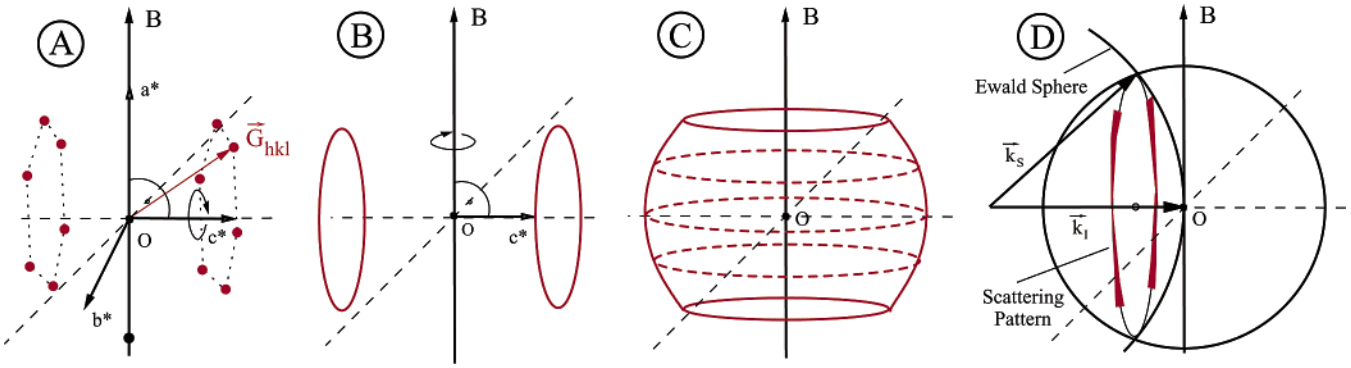

Figure 2. Reciprocal space construction of the scattering pattern caused by an (*hkl*) reflection as it is observed in WAXS measurements of a uniaxially oriented sample with perfect orientation $\vec{c} \perp \vec{B}$ and no preferred orientation of axes $\vec{a}$ and $\vec{b}$ within the plane normal to $\vec{c}$. The unit cell of the crystal is hexagonal.

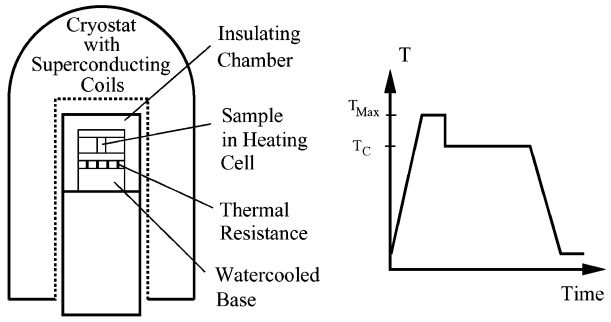

Figure 3. Probehead with a sample inside a superconducting NMR magnet and a typical temperature program for sample preparation in the magnetic field.

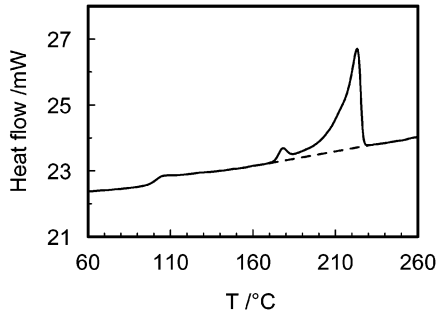

Figure 4. DSC heating scan of iPS measured with a rate of 10 K/min. Before the measurement, the sample was molten at T_{max} = 250 °C and crystallized at T_c = 165 °C. The glass transition of the remaining amorphous fraction can be seen clearly ($T_g \approx$ 100 °C). The enthalpy of melting corresponds to the area between the measured curve and the dashed line and amounts to ΔH = 28 J/g. The shape of the melting peak is very dependent on the exact thermal history of the sample.

Sample Holder. To enable crystallization with an accurately controlled temperature program, a heating cell that can be inserted into a Bruker NMR magnet (7 and 11 T) with a 74-mm bore was built. (A schematic drawing is shown in Figure 3.) A brass cell is heated by an electrical resistance heater and connected over a thermal resistor (Macor) to a watercooled base plate. Temperature is measured with a PT100 and controlled with a PID controller (Eurotherm, Limburg/Germany). The temperature calibration was checked using the melting temperature of saccharin (T_m = 228 °C) as a reference. The disk-shaped samples were held between two Kapton sheets in the oven. To prevent the oxidation of the sample, the chamber containing the heating cell was flooded with nitrogen. Two different NMR magnets with B = 7 and 11 T were used.

Wide-Angle X-ray Scattering (WAXS). For 2D-WAXS, a setup with a rotating anode (Schneider, Offenburg/Germany), operating at 6 kW, and an image plate detector (Schneider, Offenburg/Germany) was used. Cu Kα radiation was selected by a graphite monochromator. The scattering patterns (SAXS, WAXS) were analyzed with FIT2D software by A. Hammersley (ESRF, Grenoble).

Small-Angle X-ray Scattering (SAXS). SAXS measurements were performed at beamline ID2 at the ESFR in Grenoble using radiation with a wavelength λ of 1 Å. The beam size was about 0.3 mm, and a CCD camera was used as the detector.

Optical Microscopy. An Axioplan 2 microscope (Zeiss) and a Linkam hotstage (TMS 600) were used for polarized light microscopy. Pictures were taken with a digital camera.

Electron Microscopy. A LEO 912 Omega microscope, operated at 120 kV, was used for transmission electron microscopy. The samples were microtomed with a diamond blade at room temperature and were stained with ruthenium tetroxide.

Rheological Measurements. The rheological measurements were performed with a UDS 200 rheometer (Paar Physica, Austria) in parallel plate geometry.

Differential Scanning Calorimetry (DSC). Calorimetric measurements were performed with a DSC 7 (Perkin-Elmer).

Results

Thermal Program and Crystallization in the Magnetic Field. To illustrate the melting behavior of the iPS that was used, an example DSC (differential scanning calorimetry) heating scan is shown in Figure 4. The semicrystalline sample shows a glass transition around $T_g \approx$ 100 °C. A broad melting range (~170−215 °C) starting with a small peak around the temperature of the previous isothermal crystallization is typical for iPS. Underneath this signal, whose shape depends on the exact thermal history of the sample, complex melting behavior is hidden, which is often explained by subsequent melting and recrystallization processes. Nevertheless, observable melting always ends around 235 °C, far below the equilibrium melting point (T_m^∞ = 289 °C).[15] A recent analysis that offers an explanation of the complex melting in terms of structural parameters can also be found in ref 15.

A typical temperature program for crystallization is shown in Figure 3. For melting, the sample is heated to a temperature T_{max} (typically 250 °C, well above the apparent melting range), annealed for 10 minutes at T_{max}, and then quickly cooled to the crystallization temperature T_c for isothermal crystallization. The time necessary for complete crystallization at different temperatures was estimated by a series of DSC measurements shown in Figure 5. In most cases, the samples were crystallized for a period 3 times as long as τ_{max},

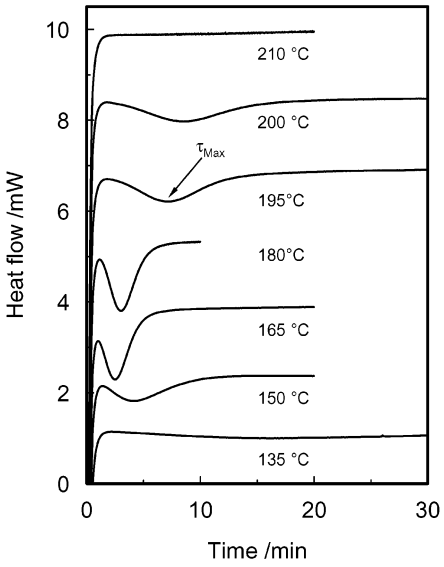

Figure 5. DSC signal versus time during the isothermal crystallization of iPS after annealing at $T_{max} = 250$ °C.

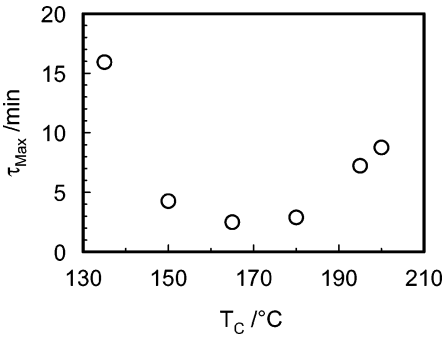

Figure 6. Times τ_{max} corresponding to the minimum in the DSC signal (maximum crystallization rate) during the isothermal crystallization of iPS after annealing at $T_{max} = 250$ °C. The data are determined from the measurements shown in Figure 5.

the time at which the maximum growth rate was observed (cf. Figure 6). For crystallization temperatures higher than $T_c = 200$ °C, where the DSC signal is too small to be observed, a crystallization time of 15 h was chosen to achieve complete crystallization. Subsequently, the samples were cooled to room temperature at a rate of 30 K/min. Because of the slow crystallization of iPS, it is possible to quench a sample below the glass-transition temperature T_g with a cooling rate as low as 5 K/min without crystallization taking place. Optical inspection after cooling therefore allows us to verify that the sample did indeed fully crystallize at T_c. After crystallization, the samples were investigated with wide-angle X-ray scattering, small-angle X-ray scattering, polarized-light microscopy, and transmission electron microscopy.

Characteristics of Magnetic-Field-Induced Orientation. As reported previously,[5] the crystallization of iPS in a strong magnetic field leads under appropriate conditions to an oriented texture with the crystal *c* axis being aligned perpendicular to the magnetic field. An example WAXS pattern is shown in Figure 7, obtained from a sample crystallized at $T_c = 210$ °C with $B = 7$ T. For comparison, a scattering pattern obtained from a sample crystallized without a magnetic field but under otherwise identical conditions is shown. The magnetic field leads to the pattern expected from the discussion

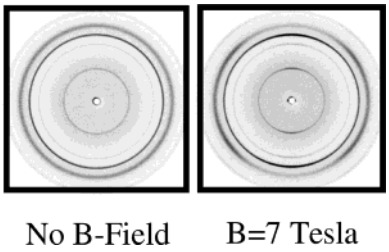

Figure 7. WAXS pattern observed from samples crystallized at $T_c = 210$ °C without and with a magnetic field ($B = 7$ T, vertical) after annealing for 10 min at $T_{max} = 250$ °C. The indices of the reflections are (110), (300), (220), and (211). The outermost ring consists of two reflections (410)/(311) and was not used for data analysis.

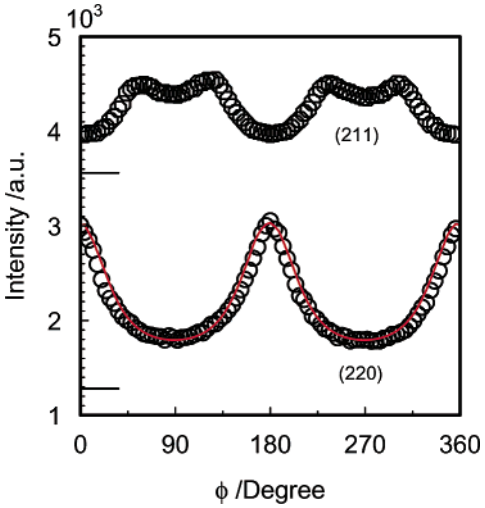

Figure 8. Azimuthal scans of (220) and (211) reflections of an iPS sample isothermally crystallized at $T_c = 200$ °C under a magnetic field of 11 T after annealing for 10 min at $T_{max} = 250$ °C. Angles $\phi = 0°$ and $\phi = 180°$ correspond to the direction of the magnetic field.

above. Another example ($B = 11$ T, $T_c = 200$ °C) is shown in Figure 8. The azimuthal scans of the (220) and (211) reflections show the shape discussed above. The continuous line corresponds to the model described in the Appendix. The orientation parameter determined in this way amounts to $S = -0.35 \pm 0.03$.

Typically, semicrystalline polymers display a hierarchy of structures, starting on a small scale with thin lamellar crystals that form approximate stacks with layers of amorphous material between.[16] On a larger scale, these lamellae branch and form spherulites. This structure is not altered by the magnetic fields, as it is shown now. Figure 9 shows a TEM image with the typical stacks of lamellae. The images look more or less identical in samples crystallized with or without a magnetic field, but after crystallization under a magnetic field, the lamellae are aligned parallel to the field, corresponding to an orientation of the chains perpendicular to the field. This kind of lamellar alignment leads to the appearance of two small-angle reflections on the equator, as shown in the inset of Figure 10. The small-angle scattering pattern can be understood in the same way as the pattern of the (00*l*) reflection discussed above. The main part of Figure 10 shows the integrated intensity as a function of the scattering vector q ($q = 4\pi/\sin\theta$, with 2θ being the scattering angle). The position and the shape of the SAXS peaks are not affected by the magnetic field. For $T_c = 210$ °C, the long

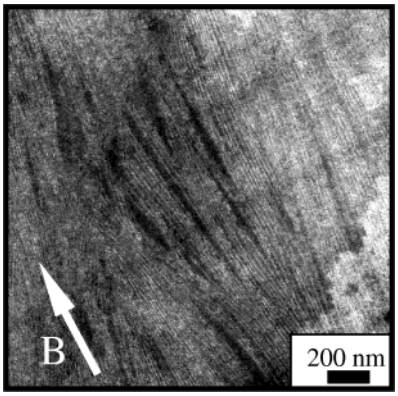

Figure 9. Electron micrograph of a highly oriented iPS. The crystallization temperature T_c was 210 °C, and direction of $\vec{B}$ is indicated. (T_{max} = 250 °C, B = 11 T).

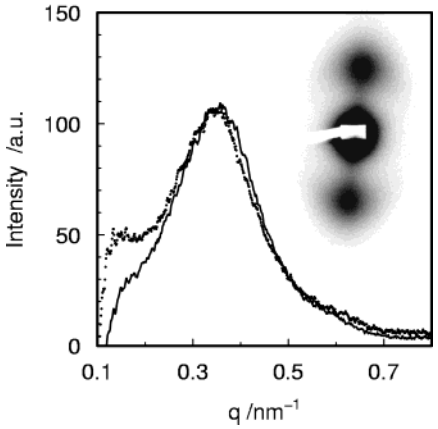

Figure 10. SAXS: Integrated intensity vs q from an isotropic sample (dotted line) and a sample aligned by crystallization in a magnetic field (T_{max} = 250 °C, T_c = 210 °C, B = 7 T, solid line). The background at low q was subtracted, and the curves were scaled to equal height at the maximum. The inset shows the 2D scattering pattern obtained from the oriented sample.

spacing amounts to $L \approx 18$ nm, in agreement with previous studies.[15]

Influence of Nucleation Density on the Extent of Orientation. The degree of orientation obtained after crystallization in a magnetic field is strongly influenced by the conditions of crystallization. Previously, it was observed (although not for iPS) that the temperature T_{max} at which the sample is heated prior to crystallization is important in this context. For a T_{max} that is too far above the apparent melting temperature, the macroscopic orientation disappears. Figure 11 shows that iPS exhibits the same behavior. Whereas for T_{max} = 250 °C, which is the condition used for all of the measurements shown above, strong magnetic-field-induced orientation is observed, a higher T_{max} of 265 °C leads to an isotropic pattern. Here, T_c and B were kept unchanged (T_c = 200 °C, B = 11 T). In both cases, the sample was fully crystallized.

These results show an intriguing correspondence to the observations by optical microscopy. It is important to realize that by changing T_{max} in the temperature range under question the density of nuclei for the subsequent crystallization is strongly altered. At lower temperatures, strong self-seeding takes place, but at the higher temperature, it is largely suppressed.[11] Obviously, magnetic-field-induced orientation can be achieved only in a crystallization process that starts from a high nucleation density. Self-seeding in iPS is illustrated by

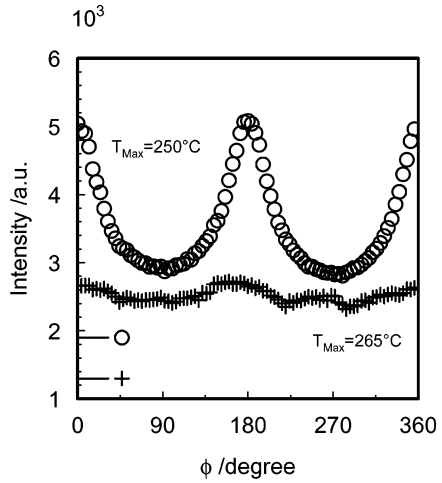

Figure 11. Intensity of the (220) reflection vs the azimuthal angle of two samples crystallized in a magnetic field (T_c = 200 °C, B = 11 T) with different thermal histories (T_{max} = 250 and 265 °C). For T_{max} = 265 °C, no orientation is observed.

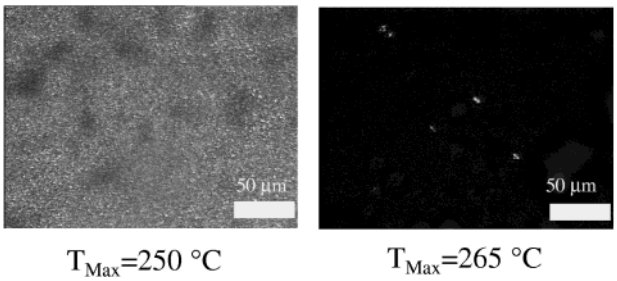

Figure 12. Optical micrographs (crossed polars) obtained from two samples crystallized at T_c = 170 °C for several minutes after different thermal histories (T_{max} = 250 and 265 °C). The density of nuclei initiating crystallization is very different for the two cases.

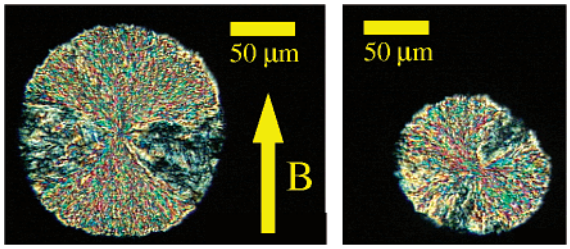

Figure 13. (Left): Micrograph (crossed polars) of an iPS spherulite grown in a magnetic field of 7 T at T_c = 220 °C after annealing at T_{max} = 260 °C. (Right): Micrograph of a spherulite grown without a magnetic field at T_c = 220 °C after annealing at T_{max} = 265 °C. The central axis of the branching spherulite is always aligned with $\vec{B}$ if a field was present during crystallization. The shape of the spherulites is not influenced by the field.

the two optical micrographs in Figure 12, which show that the number of nuclei appearing after annealing at T_{max} = 250 °C is much higher than that after annealing at T_{max} = 265 °C. For these measurements, a temperature of crystallization T_c = 170 °C was chosen to allow for a series of measurements in a reasonable time.

If crystallization takes place at low nucleation density, then large individual spherulites grow as shown in Figure 13. The spherulites contain a large anisotropic core consisting of a stack of lamellae, a so-called hedrite,[17,18] which then branches out, resulting in an isotropic, approximately spherical object. These characteristics remain unchanged if the crystallization takes

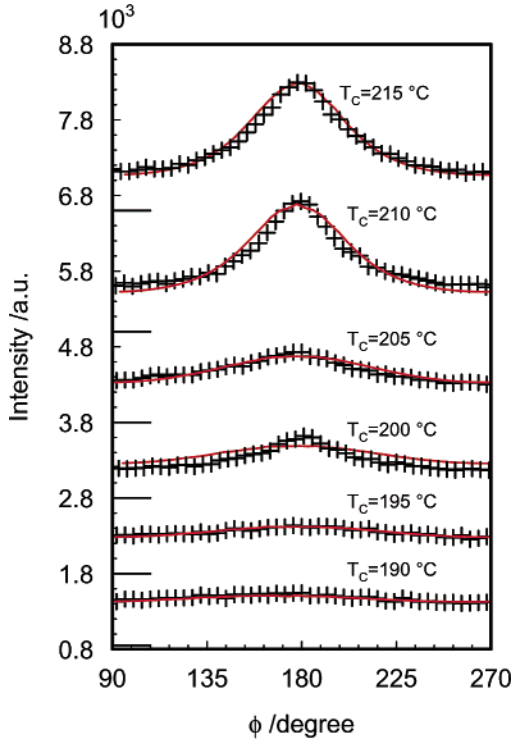

Figure 14. Azimuthal (220) WAXS scans of iPS for different crystallization temperatures T_c (T_{max} = 250 °C, B = 7 T, ϕ = 180° corresponds to the direction of B). Individual curves are shifted, and the corresponding background is indicated on the left. The solid lines are model curves calculated according to eq 9.

place under the influence of a magnetic field. The only difference is the orientation of the central part, which is oriented at random without a field but is aligned parallel to $\vec{B}$ if a field is present.

This observation suggests a simple explanation of the influence of T_{max} on the alignment. Whereas for high nucleation density the anisotropic, oriented cores of the spherulites occupy most of the volume, leading to a macroscopic orientation, this effect is lost for low nucleation density because in this case the overall random orientation of the outer parts of the spherulites dominates.

At this point, we can exclude the fact that magnetic-field-induced orientation is achieved by a direct influence on the growing crystals at the growth front of the spherulite. If this were the case, then the orientation would not be lost during spherulitic growth and the internal organization and outer shape of the spherulites would be affected by the presence of the magnetic field.

Influence of Crystallization Temperature and Field Strength on Orientation. For a given T_{max}, the orientation is further dependent on the temperature of crystallization T_c, as can be seen in Figure 14, which shows the results for a series of WAXS measurements taken from samples crystallized at different T_c values (B = 7 T, T_{max} = 250 °C). The orientation is almost perfect ($S = -0.40$) for high crystallization temperatures (T_c = 215 °C) and disappears for low temperatures (T_c = 190 °C). Manual fits with the model described in the Appendix (eq 9) are shown as solid lines. Generally, a very good description of the data can be achieved with this model; the discrepancy visible for the data set with T_c = 200 °C is the exception. Before fitting, all data sets were normalized to a common background level corresponding to the amorphous, isotropic part of the sample.

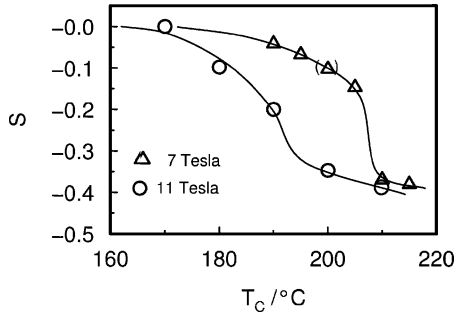

Figure 15. Orientation parameter S vs crystallization temperature T_c for field strengths B = 7 and 11 T as determined by a manual fit of the model described in the Appendix (eq 9) to data as shown in Figure 14. For all measurements, T_{max} = 250 °C. The lines are guidelines for the eye. (The point at T_c = 200 °C is in parentheses because the corresponding data set shown in Figure 14 is not very well described by the model.)

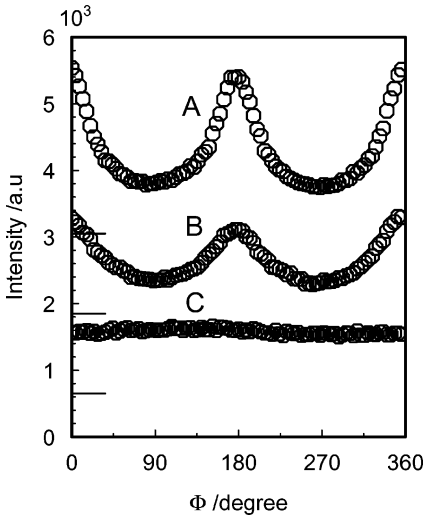

Figure 16. Azimuthal WAXS scans ((220) reflection) of iPS samples treated with the same temperature program (Figure 3, T_{max} = 250 °C, T_c = 200 °C, B = 11 T) but with different exposures to the magnetic field. Curve A: melting, annealing, and crystallization in the field. Curve B: melting and annealing outside the field and crystallization inside the field. Curve C: melting and annealing inside the field and crystallization outside the field. Curves are shifted, and the background is indicated at the left margin.

This procedure is necessary to correct for small variations in sample thickness. Then this background was subtracted, and for all curves, a common prefactor I_0 (eq 9) was used. The same procedure was applied to the data resulting from crystallization at B = 11 T. The order parameter obtained from this analysis of the WAXS data is shown in Figure 15 as a function of the crystallization temperature T_c. Whereas over a large range of T_c the orientation is improved by the stronger field of 11 T, it seems that at high crystallization temperatures ($T_c \approx$ 210 °C) saturation sets in at $S \approx -0.40$.[33]

The strong influence of the crystallization temperature on the degree of orientation suggests that the orientation process takes place during the process of crystallization itself. To test this conclusion further, an experiment was performed in which three samples were prepared with an identical thermal program but with different exposure to the magnetic field. The results are shown in Figure 16. Different from the procedure described above (melting and isothermal crystallization in the magnetic field, A), in one case the sample was

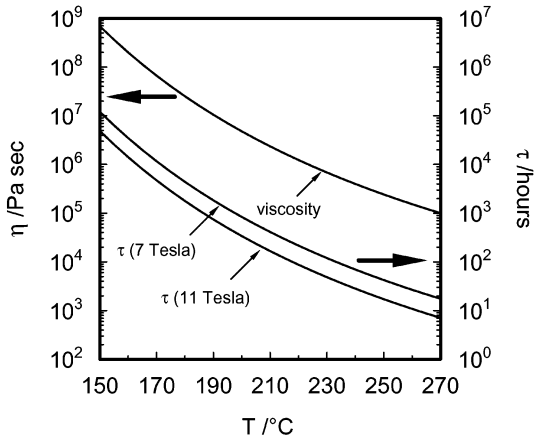

Figure 17. Zero shear rate viscosity of iPS (upper line), as extrapolated from DMA measurements at several temperatures above the melting-temperature range. The lower curves show the calculated time of rotation τ_{rot} for $B = 7$ and 11 T on the basis of eq 3.

inserted into the magnet only during cooling from T_{max} to T_c, and melting happened outside beforehand (B). In the third case, the sample was taken out of the magnet immediately after melting and annealing, at the onset of cooling to T_c, and crystallization happened outside of the magnetic field (C). Whereas no orientation is observed after procedure C, substantial orientation is achieved for procedure B ($S = -0.22$), confirming that the orientation takes place during the crystallization and not before. The different degree of orientation between A and B indicates that the alignment can begin immediately after cooling below T_{max}, when the first nuclei might start growing. If the magnetic field starts acting later, then the resulting degree of orientation is somewhat lower.[34] These observations are different from results obtained previously on iPP.[8] In that case, even a crystallization procedure similar to C led to orientation. A direct comparison, though, is somewhat difficult because for the iPP samples the crystallization happened much faster during a rapid quench.

Viscosity Measurements. To estimate the mobility of a growing hedrite in the surrounding melt, the zero shear rate viscosity $\eta_0(T)$ of our sample was determined by dynamic mechanical measurements in the molten state from the imaginary part of the shear modulus $G''(\omega)$ in the terminal flow region. Using the experimentally determined shift factor, extrapolated values at temperatures in the crystallization range could be obtained. The viscosity resulting from this procedure is shown as a function of temperature in Figure 17.

Discussion

Above we discussed a series of experiments in which a magnetic field induces orientation during the crystallization of iPS. Before discussing the mechanism of the alignment process itself, let us briefly recall the main results. As for most polymers, crystallization from the quiescent melt in iPS proceeds via the formation of spherulites, starting with the nucleation and growth of a hedritic core that later branches out to form an isotropic spherulitic object. It is only the core of the spherulite that can be oriented during crystallization in a magnetic field. Crystal growth in the outer part of the spherulite seems basically unaffected by the field. To obtain a macroscopically highly oriented sample, the size of the spherulites has to be restricted by a high nucleation density. In addition, slow crystallization at a high crystallization temperature T_c is required. Below $T_c \approx 190$ °C, no macroscopic orientation develops, with the exact temperature depending on the strength of the magnetic field. Over the range in T_c in which orientation can be achieved, the crystal growth velocity changes by about an order of magnitude. In contrast to the results obtained from previous experiments on other crystalline polymers,[8] it is important that the crystallization itself takes place in the magnetic field; a preceding annealing of the melt in the field is not sufficient.

The observations suggest that the alignment during the initial phase of spherulitic growth simply occurs by a rotation of the hedrites in the surrounding melt caused by the torque exerted by the magnetic field on this anisotropic structure. This alignment will take place independently of the number of nuclei present. But if the size of the spherulites is restricted to only the size of the hedritic core, the orientation is preserved during the whole process of growth, and macroscopic orientation occurs. Therefore, a high density of nuclei, which restricts the final size of spherulites, is crucial for macroscopic orientation. This high nucleation density can be achieved by self-seeding. In addition there has to be enough time for the hedrite to orient before the crystallization process is finished. This becomes critical for greater supercooling where the growth rate increases while the orientation process becomes slower because of increased viscosity. The initial nucleation centers themselves seem to be too small to experience orientation in the magnetic field; therefore, the alignment takes place simultaneously with growth. The suggested scenario is consistent with estimates for the size of a critical nucleus based on classical nucleation theory, which leads to typical length scales of about 10 nm,[11] well below the 70 nm estimated above to be necessary for noticeable magnetic field effects. The size of the crystal remnants might of course depend on the material under study, and this could explain why Kawai et al.[8] observed orientation before the onset of growth.

Although this picture naturally explains the main features of magnetic-field-induced orientation, a simple estimate of the time scale of rotation is actually not in agreement with our observations. Possible explanations will be discussed below. We estimate the time needed to rotate a hedrite in a simplified way by considering a sphere with diamagnetic anisotropy $\Delta\chi$ in a viscous liquid with viscosity η. The laminar flow profile can be solved for this case, and the time of rotation τ_{rot} in a magnetic field $\vec{B}$ is given by[19,20]

$$\tau_{rot} = \frac{6\eta\mu_0}{|\Delta\chi|B^2} \tag{3}$$

with $\mu_0 = 4\pi \cdot 10^{-7} N/A^2$ being the vacuum permeability. The time of rotation τ_{rot} is independent of the volume V of the sphere because the magnetic torque as well as the frictional torque are proportional to V. The frictional torque from an infinitesimal area on the surface is $d\vec{M} = \vec{R} \times d\vec{F}$, whereby the magnitude of the force $d\vec{F}$ does not depend on the radius of the sphere.[20] Because the integration over the surface of the sphere contributes a factor of R^2, $\vec{M}$ is proportional to R^3. For the magnetic torque, the factor R^3 is obvious as long as the anisotropy is homogeneous throughout the sphere. If the spherulites starts to build up an isotropic, branched

structure, then the weight of the magnetic torque decreases relative to the frictional torque, and the rotation slows down.

The time of rotation τ_{rot} can be estimated using the measured values for the viscosity. With a crystallinity of about 30%,[15] the effective anisotropy of the susceptibility for a hedrite is $\Delta\chi \approx -2.45 \times 10^{-7}$. Figure 17 shows the calculated values for τ_{rot} as a function of temperature for magnetic fields of 7 and 11 T according to eq 3. It is obvious that according to this estimate the process of rotation would take far longer than the crystallization itself (e.g., at $T_c = 200$ °C, $\tau_{rot} \approx 130$ h, but the sample crystallizes within 20 min (from DSC)). Although this calculation is based on some simplified assumptions, the discrepancy seems hard to dismiss, and we want to discuss possible explanations. First, we make a remark concerning a possible cause of experimental errors: A certain reduction in the viscosity at high temperatures due to the degradation of molecular weight cannot be completely excluded, but because the rheological experiments were performed under similar conditions, it is unlikely that such a strong discrepancy would be caused in this way. The assumption of a spherical shape for the growing spherulite should not be critical but rather should give a lower bound for τ_{rot}. It remains an assumption that the growing crystal can be treated as a solid body surrounded by a viscous melt from the very beginning of the crystallization process. The observed fast alignment would become more easily conceivable under the alternative assumption that the alignment of the growing nucleus is assisted by a large internal mobility and the ability to rearrange accordingly on a time scale more closely related to molecular relaxation times. In such a picture, one would assume that the nucleation center rather consists of a domain in the melt that is left in a preordered state after melting.[21] A similar assumption was brought forward by Kawai et al.[10] and has been discussed in the context of enhanced nucleation occurring in oriented samples.[22] Certainly these considerations are based on indirect evidence, but they could perhaps be tested directly by future experiments following the process of orientation in situ.

Conclusions

In a series of detailed experiments, we have investigated the conditions under which the crystallization of isotactic polystyrene in a strong magnetic field leads to orientation. We have confirmed that the alignment takes place during the initial stage of crystal growth. A detailed picture of the orientation process emerges from our experiments and also explains the previously observed strong influence of the thermal history of the sample. The magnetic field leads to an orientation of the crystalline material shortly after nucleation, before the development of objects with spherical symmetry, the so-called spherulites, takes place. This alignment seems to happen on a surprisingly short time scale. However, the magnetic field proves to be unable to direct growth in the branched outer part of the spherulites, which leads to macroscopically isotropic samples if large spherulites are grown. For magnetic-field-induced orientation to occur, two conditions have to be fulfilled: the crystallization has to start from a high nucleation density, and crystal growth has to be slow enough to allow for the orientation of the growing stacks of lamellae. In retrospect, it seems that this recipe has also been used on an empirical basis in previous experiments dealing with magnetic-field-induced orientation.[5−10]

The proposed mechanism of orientation seems quite different from alignment induced by external fields in systems undergoing a weak first-order transition accompanied by large fluctuations such as the disorder-to-order transition in block copolymers. Here, the growth process itself can be steered by an electric field.[23] The discrepancy between the indirectly observed time scale on which the orientation takes place and the estimates made above might be an indication that even in the case of a crystallization the alignment of the growing nucleus happens by some kind of internal rearrangement of the nucleus. This will remain speculation, though, until further observations by in-situ experiments give more direct information about the process of alignment itself. Related questions might arise for magnetic-field-induced orientation during the crystallization of proteins from solution.[24,25] In protein crystallization, the role of a transient, denser precursor structure for nucleation has been proposed to explain the unusually high nucleation rates over a certain range of the phase diagram.[26,27] One could imagine that such a mesomorphous precursor structure exhibits a high sensitivity for magnetic-field-induced alignment. Similar precursor structures are also being considered in the context of polymer crystallization.[28,29]

Acknowledgment. In the course of this work, we had very valuable discussions with G. Strobl, G. Reiter, J.-U. Sommer, B. Lotz, T. Kimura, and T. Kawai. In addition, we thank G. Strobl for his general support of the project. We are grateful to K. Saalwächter and the Institute for Macromolecular Chemistry of the Albert-Ludwigs-University-Freiburg for giving us access to their NMR magnet. We thank R. Thomann for the TEM micrographs and W. Schemionek for the rheological measurements. Furthermore, we are grateful to Volker Urban and the ESRF for giving us the opportunity to perform SAXS measurements on beamline ID2 of the ESRF. Technical help from A. Hasenhindl, B. Heck, and M. Goldmann is gratefully acknowledged. For the analysis of 2D-scattering data, we used FIT2D software written by A. P. Hammersley from the ESRF. This work was supported by the EC under contract no. HPRN-1999-00151.

Appendix

Here, we illustrate the method used in this paper to determine the orientation parameter from the azimuthal intensity variation of an ($hk0$) reflection. We assume a Gaussian orientation distribution with the preferred orientation at an angle $\pi/2$ with respect to a given direction (here the direction of the magnetic field $\vec{B}$) and with a width parameter κ defined below. Such an orientation distribution is characterized by a negative orientation parameter. We derive the azimuthal intensity $I_\kappa(\phi)$ obtained in a Debye−Scherrer-like measurement in several steps.

(1) We derive an expression for the intensity $i_\delta(\theta)$ on the sphere in reciprocal space corresponding to a given ($hk0$) reflection for the condition $\angle(\vec{c},\vec{B}) = \delta$. In reciprocal space, we use spherical coordinates (θ, Φ, r).

(2) An orientation distribution $p_\kappa(\delta)$ for the intensities $i_\delta(\theta)$ centered around $\delta = \pi/2$ is introduced, and the

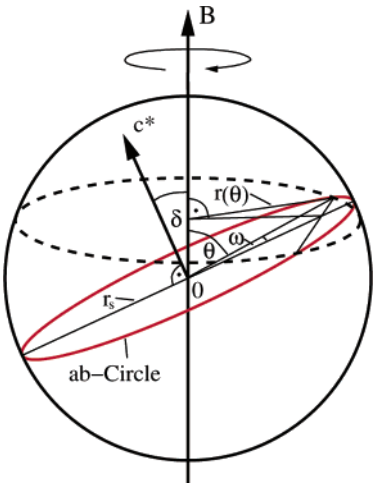

Figure 18. Reciprocal space construction of the intensity for fixed inclination angle δ between $\vec{B}$ and $\vec{c}^*$. The symbols that are used are described in the text.

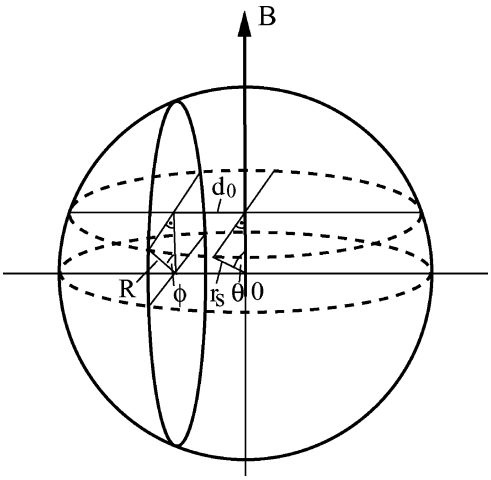

Figure 19. Density projection of reciprocal lattice vectors $\vec{G}$ from the sphere of reflection onto the circle intersecting the Ewald sphere, which corresponds to the scattering picture seen on a 2D detector. The symbols that are used are described in the text.

total intensity on the reflection sphere $i_{tot}(\theta)$ corresponding to an integral over the different values of δ is defined.

(3) The intensity $i_{tot}(\phi)$ observable in an experiment is constructed by taking the intersection of the intensity distribution in reciprocal space with the Ewald sphere. Here, ϕ is the azimuthal angle on the detector.

(4) An integration of $i_{tot}(\phi)$ over angular intervals $\Delta\phi$ yields the total intensity $I_\kappa(\phi)$, which corresponds to the intensity observable on a detector.

Step 1. For the calculation of $i_\delta(\theta)$, we assume that the c^* axis has a fixed inclination to the direction of $\vec{B}$, not necessarily equal to the preferred angle $\delta = \pi/2$. The circle in the $\vec{a}-\vec{b}$ plane made up of reciprocal lattice vectors $\vec{G}_{hk0}$ (analogous to the $\vec{a}-\vec{b}$ circle in Figure 1B) is rotated around the direction of $\vec{B}$ (Figure 18), which leads to a distribution of intensity on a belt-shaped part on the sphere of reflection around the equator. Here, $r_s = |\vec{G}_{hk0}|$ denotes the radius of the circle. The intensity on the sphere follows

$$i_\delta(\theta) \propto \frac{\left|\frac{\partial\omega_\delta(\theta)}{\partial\theta}\right|}{r(\theta)} \tag{4}$$

where $r(\theta)$ is the distance from a point on the sphere to the central axis. By rotation, every point corresponding to an angle ω on the $\vec{a}-\vec{b}$ circle is distributed on a circle on the sphere of reflection characterized by a common angle θ. Angles ω and θ are related by $\cos\theta = \cos\omega \sin\delta$, and the density on the sphere for a given θ is proportional to the derivative

$$\frac{\partial\omega_\delta(\theta)}{\partial\theta} = \frac{\sin\theta}{\sqrt{\sin^2\delta - \cos^2\theta}}$$

With $r(\theta) = r_s|\sin\theta|$, eq 4 becomes

$$i_\delta(\theta) \propto \frac{1}{\sqrt{\sin^2\delta - \cos^2\theta}} \tag{5}$$

with two integrable singularities in the interval $[0, \pi]$ at $\theta = \pi/2 - \delta$ and $\theta = \pi/2 + \delta$.

Step 2. The total density $i_{tot}(\theta)$ of vectors $\vec{G}_{hk0}$ on the sphere is given by

$$i_{tot}(\theta) \propto \int_0^1 p_\kappa(\delta) \cdot i_\delta(\theta)\, \mathrm{d}\cos\delta \tag{6}$$

where $p(\delta)$ is a weighting function for the densities $i_\delta(\theta)$ derived in step 1. We choose a Gaussian distribution

$$p_\kappa(\delta) = \frac{1}{n(\kappa)} \exp(-\kappa \cdot \cos^2\delta)$$

with a normalization factor

$$n(\kappa) = \int_0^1 \exp(-\kappa \cdot \cos^2\delta)\, \mathrm{d}\cos\delta$$

and an exponent $\kappa > 0$ describing the width of the distribution function.[35] This exponent κ is directly related to the order parameter S by

$$S = \langle P_2(\cos\delta)\rangle = \int_0^1 P_2(\cos\delta)\, p_\kappa(\cos\delta)\, \mathrm{d}\cos\delta \tag{7}$$

with the second Legendre polynomial

$$P_2(x) = \frac{3x^2 - 1}{2}$$

Step 3. In Figure 19, the projection of the intensity on the circle representing the intersection with the Ewald sphere is sketched. The relation of the azimuthal angle ϕ in detector coordinates and spherical coordinate θ in reciprocal space is

$$\cos\theta = \frac{R}{r_s}\cos\phi = \sqrt{1 - \frac{r_s^2}{4k^2}}\cos\phi \tag{8}$$

where

$$R = \sqrt{r_s^2 - d_0^2}$$

is the radius of the circle of intersection. d_0 equals $r_s^2/2k$. These relations can be obtained from the geometry sketched in Figure 1D. $k = 2\pi/\lambda$ denotes the wavevector of the X-rays used.

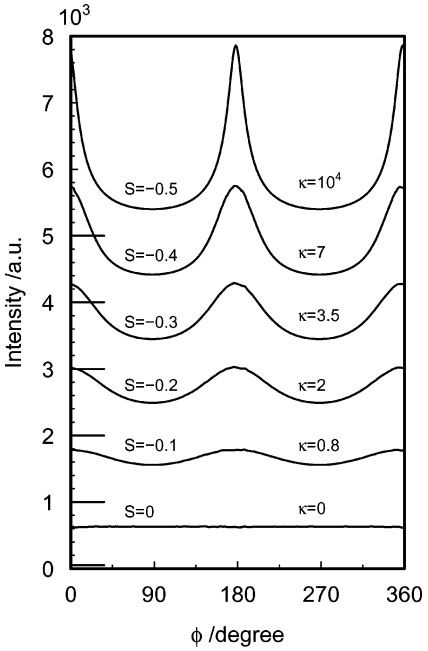

Figure 20. Calculated azimuthal scans for a (220) reflection of iPS with mean orientation $\vec{c} \perp \vec{B}$ for several degrees of orientation as indicated. The curves are shifted; the respective zero is indicated on the left.

Step 4. The total azimuthal intensity $I_\kappa(\phi)$ for a given κ follows from eqs 6 and 8 and by integration over angular intervals $\Delta\phi$. The integration here corresponds to the implicit integration carried out during measurements due to finite detector resolution. It is necessary to include this integration to flatten the integrable singularities remaining from eq 5. The azimuthal intensity for an (hk0) WAXS reflection of a uniaxially oriented system with an orientation distribution centered around $\vec{c} \perp \vec{B}$ is therefore given by

$$I_\kappa(\phi) = \frac{I_0}{n(\kappa)} \int_0^1 \mathrm{d}\cos\delta \int_\phi^{\phi+\Delta\phi} \mathrm{d}\phi' \times \frac{\exp(-\kappa \cos^2\delta)}{\sqrt{1 - \cos^2\delta - (1 - (r_s^2/4k^2))\cos^2\phi'}} \quad (9)$$

Here, I_0 is a prefactor depending on experimental details. Results of example calculations are shown in Figure 20 for several selected values of κ. For $\kappa = 0$, the curve is flat because of a lack of orientation (order parameter $S = 0$), and for very large κ (order parameter $S \approx -0.5$), the curve converges to the shape (with finite width) of the peaks in direction B and an offset as qualitatively described in Figure 1. The parameters for the curves in Figure 20 were chosen for the (220) reflection of iPS. In this case, $r_s = 4a^* \cdot \cos 30 = 1.38$ Å^{-1} ($a = b = 22.08$ Å and $c = 6.626$ Å[30]). The wavelength λ was taken as 1.54 Å (Cu Kα). The integrals in Figure 20 were numerically calculated with a simple approximation by Riemann sums. The normalization factor $n(\delta)$ is calculated via a Romberg integration.[31]

References and Notes

(1) Morkved, T.; Lu, M.; Urbas, A. M.; Ehrichs, E. E.; Jaeger, H. M.; Mansky, P.; Russell T. P. *Science* **1996**, *273*, 931.
(2) Thurn-Albrecht, T.; Schotter, J.; Kästle, G. A.; Emley, N.; Shibauchi, T.; Krusin-Elbaum, L.; Guarini, K.; Black, C. T.; Tuominen, M. T.; Russell T. P. *Science* **2000**, *29*, 2126.
(3) Schäffer, E.; Thurn-Albrecht, T.; Russell, T. P.; Steiner, U. *Nature* **2000**, *403*, 874.
(4) Sata, H.; Kimura, T.; Ogawa, S.; Yamato, M.; Ito, E. *Polymer* **1996**, *37*, 1879.
(5) Ezure, H.; Kimura, T.; Ogawa, S.; Ito, I. *Macromolecules* **1997**, *30*, 3600.
(6) Sata, H.; Kimura, T.; Ogawa, S.; Ito, E. *Polymer* **1998**, *39*, 6325.
(7) Kimura, T.; Kawai, T.; Sakamoto, Y. *Polymer* **2000**, *41*, 809.
(8) Kawai, T.; Kimura, T. *Polymer* **2000**, *41*, 155.
(9) Kawai, T.; Kimura, T. *Macromolecules* **2000**, *33*, 8421.
(10) Kawai, T.; Sakamoto, Y.; Kimura, T. *Mater. Trans.* **2000**, *41*, 955.
(11) Wunderlich, B. *Macromolecular Physics*; Academic Press: New York, 1976; Vol. 2.
(12) Buchanan, D. R.; Miller, R. L. *J. Appl. Phys.* **1966**, *37*, 4003.
(13) Greis, O.; Xu, Y.; Asano, T.; Petermann, J. *Polymer* **1989**, *30*, 590.
(14) de Jeu, W. H. *Physical Properties of Liquid Crystalline Materials*; Gordan and Breach Science Publishers Inc.: New York, 1980.
(15) Strobl, G.; Al-Hussein, M. *Macromolecules* **2002**, *35*, 1672.
(16) Strobl, G. R. *The Physics of Polymers*; Springer: Berlin, 1997.
(17) Vaughan, A. S.; Bassett, D. C. *Polymer* **1985**, *26*, 717.
(18) Vaughan, A. S.; Bassett, D. C. *Polymer* **1988**, *29*, 1397.
(19) Kimura, T.; Yamato, M.; Koshimizu, W.; Koike, M.; Kawai, T. *Langmuir* **2000**, *16*, 858.
(20) Happel, J.; Brenner, H. *Low Reynolds Number Hydrodynamics*; Prentice Hall Inc.: London, 1965.
(21) Alfonso, G. C.; Zabicki, A. *Colloid Polym. Sci.* **1995**, *273*, 317.
(22) Alfonso, G. C.; Scardigli, P. *Macromol. Symp.* **1997**, *118*, 323.
(23) Thurn-Albrecht, T.; DeRouchey, J.; Russell, T. P.; Kolb, R. *Macromolecules* **2002**, *35*, 8106.
(24) Sakurazawa, S.; Kubota, T.; Ataka, M. *J. Cryst. Growth* **1999**, *196*, 325.
(25) Astier, J.-P.; Veesler, S.; Boistelle, R. *Acta Crystallogr., Sect. D* **1998**, *54*, 703.
(26) ten Wolde, P.-R.; Frenkel, D. *Science* **1997**, *277*, 1975.
(27) Anderson, V. J.; Lekkerkerker, H. N. W. *Nature* **2002**, *416*, 811.
(28) Strobl, G. *Eur. Phys. J. E* **2000**, *3*, 165.
(29) Heeley, E. L.; Maidens, A. V.; Olmsted, P. D.; Bras, W.; Dolbnya, I. P.; Fairclough, J. P. A.; Terrill, N. J.; Ryan, A. J. *Macromolecules* **2003**, *36*, 3656.
(30) Immergut, E. H.; Brandrup, J. *Polymer Handbook*, 2nd ed.; Wiley-Interscience: New York, 1975.
(31) Press: W. H.; Teukolsky, S. A.; Vetterling, W. T.; Flannery, B. P. *Numerical Recipes*; Cambridge University Press: New York, 1986.
(32) We used $\Delta\chi = [3\Delta\chi_{M,phenyl}(\cos\alpha - \sin\alpha)]/N_a V_c$. Here, $\Delta\chi_{M,phenyl} = -0.751 \times 10^{-9}$ m^3/mol.[14] V_c is the volume of the unit cell, N_a is Avogadro's number, and with $\alpha = 19.47°$ the angle between the carbon backbone and the phenyl unit is taken into account.
(33) As a side remark, it should be mentioned that it is not possible to orient iPS for crystallization temperatures as low as $T_c = 135$ °C, at which temperature the rate of crystallization is comparable to the one measured at high temperatures at which strong orientation occurs (cf. DSC measurements shown in Figures 5 and 6).
(34) Because inserting the sample holder into the magnet is an operation that takes some time, the temperature at which the magnetic field starts to act in case B is not exactly known.
(35) Note that with $\kappa < 0$ the orientation distribution for a fiber, centered around $\delta = 0$, is obtained. The same procedure as the one described here can be used in that case to describe the intensity distribution in the fiber diagram.

MA034760G